Reconciliation of the paleo sea-level record with modern crustal uplift of Greenland

Surendra Adhikari[a,1], Lambert Caron[a], Glenn A. Milne[b], Shfaqat A. Khan[c], Kristian K. Kjeldsen[d], Johan Nilsson[a], Eric Larour[a], Erik R. Ivins[a]

[a]Jet Propulsion Laboratory, California Institute of Technology, Pasadena CA, USA.
[b]Department of Earth and Environmental Sciences, University of Ottawa, Ottawa ON, Canada.
[c]Department of Geodesy and Earth Observations, Technical University of Denmark, Kgs. Lyngby, Denmark.
[d]Geological Survey of Denmark and Greenland, Copenhagen, Denmark.

[1]To whom correspondence should be addressed: adhikari@jpl.nasa.gov

Abstract [150 words]

The observed crustal uplift rates in Greenland are caused by the combined response of the solid Earth to both ongoing and past surface mass changes. Existing elastic Earth models and Maxwell linear viscoelastic GIA (glacial isostatic adjustment) models together underpredict the observed uplift rates. These models do not capture the ongoing mantle deformation induced by significant ice melting since the Little Ice Age. Using a simple Earth model within a Bayesian framework, we show that this recent mass loss can explain the data-model misfits but only when a reduced mantle strength is considered. The inferred viscosity for sub-centennial timescale mantle deformation is roughly one order of magnitude smaller than the upper mantle viscosity inferred from GIA analysis of geological sea-level data. Reconciliation of geological sea-level and modern crustal motion data may require that the model effective viscosity be treated with greater sophistication than in the simple Maxwell rheological paradigm.

Plain language summary [200 words]

There are 57 permanent Global Navigation Satellite System (GNSS) stations on bedrock in Greenland. These stations provide point-measurements of three-dimensional crustal motion. We can model a large portion of the observed crustal uplift rates as elastic Earth response to ongoing rates of ice-mass loss. We model the remaining part of the uplift rates as the ongoing viscous response of the solid Earth to past ice-ocean mass exchange -- a process termed glacial isostatic adjustment (GIA). Earth structure and deglaciation history in GIA models are usually constrained by geological data such as paleo sea level and ice margins. To fully explain the GNSS-measured uplift rates, we propose that these geologically constrained GIA models should additionally resolve: (1) ice-mass changes during and after the Little Ice Age; and (2) broadband mantle relaxation processes. While such features are challenging to implement, they offer a more granular model paradigm appropriate to the improved temporal sampling that the collective geological and geodetic data sets now provide.

Highlights [3 bullets, 140 characters each]

- GIA models constrained by paleo sea-level data underpredict the modern crustal uplift rates corrected for the elastic loading effects.
- Mass loss since the Little Ice Age can explain the residual uplift rates provided a reduced mantle strength on sub-centennial timescales.
- Reconciling geological and modern geodetic data requires a more sophisticated mantle rheology model than generally used in loading studies.

1. Introduction

There are 57 permanent Global Navigation Satellite System (GNSS) stations placed on the bedrock along the periphery of the Greenland Ice Sheet (GrIS). This network of GNSS stations -- known as GNET (Bevis et al., 2012; Khan et al., 2016) -- provides point measurements of 3-D bedrock motion. Some of these stations have been in operation since 1995, providing a valuable dataset for probing causal relationships between ice load and solid-Earth deformation over a range of timescales. Interannual, seasonal, or shorter timescale GNET signals are interpreted as an elastic response of the solid Earth to short-period surface mass changes in Greenland, including fluctuations in mass transport through outlet glaciers and atmospheric pressure variability (e.g., Bevis et al., 2012; Adhikari et al., 2017; Zhang et al., 2019). The bedrock uplift as measured by GNET is also shown to track the apparent acceleration of ice mass change that is ongoing in Greenland (Bevis et al., 2019). Geophysical interpretation of secular trends in vertical bedrock motion -- henceforth termed “uplift rates” -- is ambiguous (e.g., Simpson et al., 2011; Khan et al., 2016; van Dam et al., 2017; Milne et al., 2018). We seek to reduce this ambiguity through improved quantification of the relative contributions of contemporary (elastic) and past (viscous) load changes to the measured uplift rates (Figure 1a), especially those associated with the emergence of Greenland from the Little Ice Age (LIA).

The observed secular uplift rates in Greenland is primarily driven by surface loading phenomena. Of prime importance is climate-driven transport of ice and water mass between the continents and the ocean over a range of timescales. These include the ongoing mass loss from the GrIS and peripheral glaciers since the LIA maximum (Kjeldsen et al., 2015; Marzeion et al., 2015; Mouginot et al., 2019; Khan et al., 2020; The IMBIE Team, 2020), and the deglaciation of Greenland and nearby ice sheets during the Late Quaternary and Holocene and the associated change in relative sea-level (RSL) (e.g., Tarasov and Peltier, 2002; Fleming and Lambeck, 2004; Simpson et al., 2009; Tarasov et al., 2012; Lecavalier et al., 2014). The response of the solid Earth to these surface loads is typically modeled by considering elastic Earth deformation due to present-day surface mass changes and a delayed viscous response of the mantle induced by past load changes, a process referred to as glacial isostatic adjustment (GIA). The existing GIA models constrained by paleo RSL data generally do not fit the uplift rates corrected for the elastic loading effects (Simpson et al., 2011; Khan et al., 2016; van Dam et al., 2017; Milne et al., 2018).

Our main goal here is to better understand this general inconsistency between the observed and modeled uplift rates in Greenland through a closer examination of the model-predicted viscoelastic Earth deformation. We determine an improved elastic contribution by incorporating the present-day surface mass changes at kilometer-scale resolution and producing uncertainty estimates of both the surface load and the elastic Earth structure. We also develop an improved GIA model by considering ice mass changes since the Medieval Warm Period (MWP) that preceded the LIA, which are either omitted or poorly represented in previous studies (e.g., Simpson et al., 2009; Lecavalier et al., 2014; Peltier et al., 2015; Wake et al., 2016; Milne et al., 2018).

2. Elastic uplift rates

Satellite altimetry and gravimetry measurements have provided unprecedented constraints on the spatiotemporal distribution of Greenland ice mass change over the past three decades (Mouginot et al., 2019; Sasgen et al., 2020; The IMBIE Team, 2020). CryoSat-2 measurements of surface elevation

change are available at a kilometer-scale resolution. From these, we estimate that Greenland, including peripheral glaciers, has lost ice mass at an average rate of 237 ± 47 Gt/year between January 2011 and December 2016. We use the methods of Nilsson et al. (2016) to process the satellite altimetry data and apply an appropriate correction for firn air content based on the Regional Atmospheric Climate Model (RACMO) predictions (Noël et al., 2016). Figure 1a shows the spatial pattern of the rate of ice height change during 2011-2016. The modeled uplift rates at GNSS stations are sensitive to the spatial structure of the surface mass changes (Adhikari et al., 2017). It is, therefore, essential to resolve these surface changes with a high level of spatial fidelity. For improved predictions of the elastic uplift, it is also important to consider contemporary mass changes in adjacent areas, especially those occurring in the Canadian Arctic where significant amount of ice has been lost recently (Wouters et al., 2019). Here we consider the surface mass changes in the adjacent areas based on the Gravity Recovery and Climate Experiment (GRACE) data (Watkins et al., 2015; Adhikari et al., 2019). Rates of Greenland and adjacent mass changes and uncertainties therein are shown in Supplementary Figure S1.

A seismologically constrained, radially stratified, 1-D Preliminary Reference Earth Model (PREM) (Dziewonski and Anderson, 1981) has been the standard model for surface loading studies, although more realistic models based on considerably denser teleseismic ray sampling are available for the upper mantle and crust. Cammarano et al. (2005), for example, utilize seismic and mineral physics constraints to deduce 99 plausible 1-D profiles for the upper mantle and transition zone from global seismic data. Similarly, Laske et al. (2013) provide a $1° \times 1°$ gridded global shallow elastic Earth structure resolving three sediment layers and three underlying layers of crystalline crust. These models are critical to regional loading studies, as they define short-wavelength features that may influence the predicted uplift rates. The Laske et al. (2013) inferences of both density and Poisson's ratio in Greenland, averaged over the upper 50 km of solid Earth, are each smaller than corresponding values from PREM by several percent (Supplementary Figure S2). We combine PREM with more recent upper mantle (Cammarano et al., 2005) and crustal (Laske et al., 2013) models to generate a total of 640 1-D elastic Earth models. The model ensemble provides a better approximation of the regional elastic and density structure than does PREM. It also captures the uncertainties that can be propagated into modeled uplift rates for Greenland. Given 1-D profiles of density and Lamé parameters, we solve a linear system of equations for the perturbations in motion and gravitation subjected to appropriate boundary conditions in order to calculate the so-called load Love numbers (Longman, 1962). We define corresponding Green's functions (Farrell, 1972) that can be convolved with surface loads to calculate the elastic bedrock motion (Adhikari et al., 2017). We perform benchmark experiments for PREM and compare them to our regionally adapted elastic Earth models, both in terms of Love numbers and the modeled uplift rates (Supplementary Figure S2).

Our estimates of both the elastic uplift rates and uncertainties are shown in figures 1b-c. On average, the Greenland crust experienced uplift during 2011-2016. The central east region, however, subsided at a small rate of $\sim$1 mm/year. The highest uplift rates are found along the ice margin and in the ablation zone and generally decrease toward both the ocean and the inland, reflecting the spatial pattern of the measured ice thinning rates (Figure 1a). Mass changes in the adjacent regions contribute to uplift at a peak rate of $\sim$1 mm/year in the northwest but are generally negligible elsewhere in Greenland (Supplementary Figure S3). Our uncertainty estimate combines those associated with both the surface load and elastic Earth structure. For ice thickness change, both measurement and instrument uncertainties are quantified (Nilsson et al., 2016), as well as those associated with the model-based estimate of firn air content (Noël et al., 2016). The uncertainty in mass change in the adjacent areas is

taken from Adhikari et al. (2019). We find that the solid Earth model uncertainty is generally smaller than the absolute bias in the modeled uplift rates relative to PREM and that the surface load, rather than the elastic Earth structure, is the dominant source of uncertainty in the modeled uplift rates (Supplementary Figure S3).

3. GIA and residual uplift rates

Model reconstructions of Greenland and nearby ice sheets during the late Quaternary and Holocene are constrained by a suite of geological and geodetic data sets (e.g., Tarasov and Peltier, 2002; Fleming and Lambeck, 2004; Tarasov et al., 2012; Lecavalier et al., 2014). These reconstructions are often limited in spatial and temporal resolution, although high spatiotemporal reconstructions are becoming available at least for part of Greenland (Cuzzone et al., 2019; Briner et al., 2020). Of particular relevance to this study is that surface load changes on decadal to century timescales are not well captured in GIA models. Previous GIA modeling studies have generally utilized available RSL data in order to constrain solid Earth properties, especially the 1-D radial profile of mantle viscosity (e.g., Lambeck et al., 2014, 2017; Lau et al., 2016; Caron et al., 2018). While regional geophysical data reveal significant lateral variability in Earth structure beneath Greenland (Darbyshire et al., 2018; Pourpoint et al., 2018; Steffen et al., 2018), to our knowledge, no GIA studies have yet incorporated these constraints in 3-D Earth models. Milne et al. (2018) determined a small number of plausible 3-D Earth structures using constraints from global models of seismic velocity (Ritsema et al., 2011; Schaeffer and Lebedev, 2013; Auer et al., 2014; French and Romanowicz, 2014) and lithosphere thickness (Zhong et al., 2003; Conrad and Lithgow-Bertelloni, 2006) and investigated their impact on the modeled deglacial RSL changes and modern crustal uplift rates.

The modeled uplift rates and associated uncertainties from Milne et al. (2018) are shown in Supplementary Figure S4. These solutions account for part of the uncertainty associated with the lateral Earth structure and do not account for that associated with the deglaciation history. Large subsidence is predicted in southwest Greenland owing to the mid to late Holocene ice-sheet readvance and the forebulge collapse associated with the North American ice sheets (Lecavalier et al., 2014 and references therein), while considerable uplift is predicted in the north. This pattern is also evident in 1-D model solutions (e.g., Simpson et al., 2011; Wake et al., 2016; The IMBIE Team, 2020), implying that GIA models for Greenland constrained by geological data sets are in broad agreement, at least, in terms of the spatial pattern of modeled uplift rates. We combine the model output of Milne et al. (2018) with the improved elastic uplift rates (Section 2) and find large disagreement with the observed rates at virtually all GNET stations (Figure 1d). The data-model misfit is as much as 3-5 mm/year at many stations in the central west and southeast Greenland. These residuals, which have also been reported in previous studies (Simpson et al., 2011; Khan et al., 2016; van Dam et al., 2017; Milne et al., 2018), are much larger than the observational uncertainty at most sites and therefore require an additional geophysical explanation.

Following Simpson et al. (2011), we hypothesize that the ongoing solid Earth response to the post-MWP load changes, especially the post-LIA mass loss, explains the residual uplift rates (Figure 1d). Despite the significant amount of mass being lost from Greenland over the past ~150 years (Kjeldsen et al., 2015; Marzeion et al., 2015; Khan et al., 2020), this recent deglaciation sequence is generally not accurately accounted for in ice sheet reconstructions tuned to geological RSL observations.

4. Post-MWP loading and solid Earth response

Kjeldsen et al. (2015) provide a reconstruction of the post-LIA mass balance of the GrIS by investigating digital elevation models based on aerial imagery and historical maps with remarkable detail along much of the ice sheet periphery. They also utilize modern geodetic measurements of airborne and satellite altimetry to estimate ice sheet mass balance during the periods 1983-2003 and 2003-2010. The historical mass balance of Greenland peripheral glaciers has been modeled based on reconstructed climate data and found to be consistent with observations of glacier mass balance and ice volume change (Marzeion et al., 2015). This reconstruction reveals that more than three-quarters of total glacier mass loss since the LIA occurred during 1925-1965 (Supplementary Figure S5). We combine the ice sheet and peripheral glacier data to construct a time series of the post-LIA ice thickness anomaly, relative to AD 2016, assuming linear changes in thickness over the periods: LIA-1925, 1925-1965, 1965-1983, 1983-2003, 2003-2011, and 2011-2016 (Figure 2). As the spatial pattern of glacier mass evolution is not available, we distribute the mass anomaly (Marzeion et al., 2015) uniformly over the present-day glacier surface area as defined in the Randolph Glacier Inventory version 5.0 (Pfeffer et al., 2014). To encompass the entirety of the LIA period in our load model, we extend the loading history back to the preceding MWP (to be discussed later) whose median year is assumed to be AD 1000 (Figure 2a).

We explore the contribution of this recent loading sequence to present-day uplift rates with the aim of explaining the above-noted data-model residuals. GIA modeling approaches generally tune the viscosity structure of the mantle in order to fit geological data sets, especially the paleo RSL data that span the past ~20,000 years. In Greenland, inferred values for the upper mantle viscosity are on the order of 5×10^{20} Pa s (Fleming and Lambeck, 2004; Simpson et al., 2009; Lecavalier et al., 2014). For this value of mantle viscosity, the post-MWP mass changes (Figure 2) yield present-day uplift rates at the sub-millimeter per year level (Supplementary Figure S6). These results are relatively insensitive to the chosen lithosphere thickness and are consistent with previous studies (Simpson et al., 2011). We conclude that including a viscosity structure that is typically inferred in GIA analysis of RSL data does not result in uplift rates associated with the post-MWP loading that are large enough to explain the data-model misfits. We therefore postulate the importance of alternative mantle relaxation processes that are either governed by inherently transient rheology (Ivins et al., 2020, Lau et al., 2020) or by non-linear stress-dependent rheology (Blank et al., 2021). Such enhancement of the relaxation process acts to lower the effective viscosity on timescales of decades to centuries and thus produces more rapid uplift rates for post-MWP mass changes. To a first approximation, the possibility of reduced mantle strength can be tested using any Maxwell model (e.g., Nield et al., 2014; Barletta et al., 2018). Here we consider an incompressible half-space Earth deformation model with an elastic lithosphere over a Maxwell mantle rheology (Ivins and James, 1999; Adhikari et al., 2014), which places an upper bound on the effective viscosity reduction required to reconcile RSL and GNSS data sets (to be discussed later).

We explore model parameter tradeoffs within the formal Bayesian framework. We independently vary a total of six parameters within their respective plausible ranges: lithosphere thickness, mantle viscosity, and four parameters related to the deglaciation history (Figure 2). The latter set of parameters include (1) LIA inception time; (2) LIA termination time; (3) amplitude of the mass anomaly during LIA; and (4) amplitude of the mass anomaly during the MWP.

The duration and timing of the LIA can vary considerably from glacier to glacier, even within the same fjord system. For example, in Nuuk fjord in southwest Greenland, the marine-terminating Kangiata Nunaata Sermia was at its LIA maximum extent at 1761 and had already retreated ~5 km by 1808 (Lea et al., 2014), while the nearby Narsap Sermia remained close to its LIA maximum extent until as late as the early 2000s (Motyka et al., 2017). Due to a lack of such a comprehensive record for many glaciers, it is not feasible to consider glacier-specific timings of the LIA. Several lines of evidence based on geological, archeological, lake sediment, and ice core studies suggest that most of the Greenland glaciers advanced to their maximum extents sometime in the period 1400-1900 (e.g., Grove, 1988; Fischer et al., 1998; Kelly and Lowell, 2009; Larsen et al., 2015; Woodroffe et al., 2017). While the LIA inception time is relatively uncertain, which we consider here to vary between 1350 and 1500, the termination time is generally better constrained through a combination of above-noted data sets. In various sectors of Greenland, glaciers began a retreat from their respective maximum extents at various times, roughly centered around 1850-1900. For example, Jakobshavn Isbræ in the central west began to retreat from its maximum extent before 1850 (Briner et al., 2011; Khan et al., 2015), while Helheim and Kangerdlugssuaq glaciers in the southeast began to retreat since ~1930 (Khan et al., 2014). We consider this parameter (i.e., termination time) to vary with a Gaussian prior centered at AD 1875 having a standard deviation of 50 years. Due to modern geodetic measurements and modeling capabilities, the ice thickness change since 1983 has been quantified with relatively little ambiguity. The ice thickness anomaly during the LIA has relatively large uncertainty. A total of $14{,}862 \pm 3{,}758$ Gt of LIA mass anomaly is estimated for the GrIS and peripheral glaciers (Kjeldsen et al., 2015; Marzeion et al., 2015). We consider this parameter to vary with a Gaussian prior estimate. We assume that the ice thickness, and by inference the mass, does not evolve during the LIA. Finally, we bound the MWP ice mass to be no less than the present-day value and no more than that during the LIA (Figure 2a).

We simulate an ensemble of 3,000 1-D viscoelastic Earth model simulations. Each model considers a unique ice load history and solid Earth parameters sampled by a simulated annealing algorithm (Caron et al., 2018). Based on the predicted uplift rates, we construct a misfit function for each model as follows

$$J_i = \frac{m_i - d_i}{\sigma_i}, \tag{1}$$

where m_i and d_i are the model prediction and the target value (i.e., the residual uplift rate) at the i-th data point, respectively, and σ_i is the associated data uncertainty. We have a total of $N_{data} = 55$ constraining data points (Figure 1d). We construct the model likelihood function, L, as follows

$$L = \exp\left(-\frac{1}{2N_{data}} \sum_{i=1}^{N_{data}} J_i^2\right), \tag{2}$$

which represents the likelihood of a given model to explain the target uplift rates and, hence, serves as a weighting factor in our statistics of the model parameters and the predicted uplift rates. Given a multivariate Gaussian prior, the posterior probability, p, that updates our prior state of knowledge with information gained during the inversion (i.e., the likelihood function) is given by

$$p \propto L \ \exp\left(-\frac{1}{2}(\mathbf{x}-\boldsymbol{\mu})\ \mathbf{E}^{-1}(\mathbf{x}-\boldsymbol{\mu})^{\mathrm{T}}\right). \tag{3}$$

Here $\mathbf{x}$ is the row vector of parameter values that have Gaussian priors (see Figure 2a), $\boldsymbol{\mu}$ is the corresponding vector of prescribed parameter means, and $\mathbf{E}$ is the covariance matrix. We assume these parameters to be independent of one another, or, in other words, with correlation coefficients equal to zero.

Posterior probability density functions (PDFs) projected into 2-D spaces formed by each pair of parameters are shown in Supplementary Figure S7. We find that our solutions are insensitive to two of the most uncertain parameters: the MWP ice mass anomaly and the LIA inception time. The solution is also insensitive to the lithosphere thickness, although it has a slight trade-off with mantle viscosity. Posterior statistics of the LIA mass anomaly ($14{,}860 \pm 2{,}670$ Gt) and the termination time (AD 1865 ± 30) are not much different from those of the prior PDFs in terms of their means, although they exhibit reduced variance in both cases. One feature that stands out in the posterior PDFs is the correlation between the LIA mass anomaly and the mantle viscosity. Models with larger LIA mass anomaly perform better when the mantle viscosity is also larger. Given our knowledge of the LIA mass anomaly and its uncertainty (Kjeldsen et al., 2015; Marzeion et al., 2015), we find the preferred mantle viscosity to be in the range of $6 - 11 \times 10^{19}$ Pa s, which is smaller than the local upper mantle viscosity inferred in Greenland GIA studies by a factor of 4-8 (Fleming and Lambeck, 2004; Simpson et al., 2009; Lecavalier et al., 2014). Had our Earth structure model included increases in viscosity with depth, our preferred values for the asthenospheric environment would be even lower. Indeed, a 3-layer spherical Earth model featuring a 120-km thick lithosphere and 2×10^{21} Pa s lower mantle viscosity (Lecavalier et al., 2014) yields the upper mantle viscosity value of 3×10^{19} Pa s (Supplementary Figure S8).

5. Improved GIA uplift rates

Figures 3a-b show the expected uplift rates and associated uncertainties that are attributable to the post-MWP load changes. Large uplift rates of order 3-5 mm/year are predicted along the coastal margins in the west and southeast. While at many GNET stations our predictions are within 1-σ uncertainties of target values, there are a few stations where we fail to predict the uplift rates even within 3-σ uncertainties (Supplementary Figure S9). Our attempt to vary regional deglaciation history independently (see Figure 1a for the regional outline) does not reduce the misfit. A more granular deglaciation history than is presented here might be possible as the constraining data are improved (e.g., Briner et al., 2020). Furthermore, we have hardly exhausted the full list of additional complexities to invoke in the underlying constitutive approximations governing the deforming solid Earth (e.g., Lau and Holtzman, 2019; Ivins et al., 2020; Blank et al., 2021). One result, nevertheless, is inescapable: incorporation of the post-MWP load model coupled to an upper mantle of reduced creep strength compared to values found in previous GIA studies substantially improves the overall GNSS data fit (compare figures 3c versus 3d).

Our uplift rates associated with the post-MWP loading (figures 3a-b) are combined with the deglacial uplift rates (Supplementary Figure S4) to give a comprehensive picture of the ongoing (viscous) solid Earth deformation induced by past load changes (Supplementary Figure S10). The combined uplift rate -- termed “improved” GIA uplift rate -- at the KULU station in southeast Greenland is 4.71 ± 0.93 mm/year, which is consistent with the estimate of van Dam et al. (2017) who deduce the corresponding uplift rate to be 4.49 ± 1.44 mm/year from GNSS and absolute gravity data. The agreement is important as the data combination method used by van Dam et al. (2017) uniquely isolates the relative contributions of contemporary (elastic) and past (viscous) load changes to the GNSS rate.

The improved GIA uplift rates have ramifications for reinterpreting ice-sheet mass balance from space gravimetry. For example, a recent reanalysis of the first three years of the GRACE mission data (2002-2005) determined mass balance during that period at roughly -180 Gt/year (Velicogna et al., 2020). The

improved GIA correction developed here increases that estimate by more than 10% to near −200 Gt/year (Supplementary Table S1). The increase is due to the more robust GIA-related positive trend in geoid change -- primarily owing to the post-LIA ice mass loss and associated sub-centennial timescale mantle deformation -- and is consistent with the estimates of Khan et al. (2016) and Sasgen et al. (2020) who provide direct GNSS constraints to their GIA models.

6. Conclusion

Previous efforts to explain the modern crustal uplift rates in Greenland have considered the elastic response of solid Earth to contemporary surface mass changes and the viscous deformation of mantle induced by deglaciation of Greenland and nearby ice sheets during the Late Pleistocene and Holocene (Khan et al., 2016; Milne et al., 2018). What has been missing in these studies is the consideration of the ongoing solid Earth response to more recent mass loss following the Little Ice Age (Simpson et al., 2011; Kjeldsen et al., 2015). Here we show that the consideration of this recent loading history results in uplift rates that are sufficient to explain the majority of data-model misfits but only when a relatively reduced mantle strength is considered. The viscosity for sub-centennial timescale mantle deformation resolved by our constraining data is roughly one order of magnitude smaller than the upper mantle viscosity typically inferred in GIA analysis of relative sea-level data. Future glacial loading studies should, therefore, consider a broadband mantle rheological model that captures mantle relaxation across a range of timescales (Caron et al., 2017; Lau and Holtzman, 2019; Ivins et al., 2020, Lau et al., 2020; Blank et al 2021). Laboratory experiments of rock creep at high temperature and pressure environments (e.g., Faul and Jackson, 2015; Kohlstedt and Hansen, 2015) and recent studies of post-seismic mantle flow (e.g., Pollitz, 2019; Muto et al., 2019; Liu et al., 2020) suggest the necessity of considering such higher-order constitutive relations.

Acknowledgements

The majority of this research was carried out at the Jet Propulsion Laboratory, California Institute of Technology, under a contract with the National Aeronautics and Space Administration. GNET data used in this study can be downloaded from the DTU space repository: ftp://ftp.spacecenter.dk/pub/abbas/GNET/v1. All of the model results produced in this study will be made available at JPL's Virtual Earth System Laboratory (https://vesl.jpl.nasa.gov/) in due course.

References

Adhikari S., et al. (2014) Future Antarctic bed topography and its implications for ice sheet dynamics. *Solid Earth*, 5:569—584.

Adhikari S., et al. (2017) Mass transport waves amplified by intense Greenland melt and detected in solid Earth deformation. *Geophysical Research Letters*, 44:4965—4975.

Adhikari S., et al. (2019) Sea-level fingerprints emergent from GRACE mission data. *Earth System Science Data*, 11:629—646.

Auer L., et al. (2014) Savani: A variable resolution whole-mantle model of anisotropic shear velocity variations based on multiple data sets. *Journal of Geophysical Research*, 119:3006—3034.

Barletta V., et al. (2018) Observed rapid bedrock uplift in Amundsen Sea Embayment promotes ice-sheet stability. *Science*, 360(6395):1335—1339.

Bevis M., et al. (2012) Bedrock displacements in Greenland manifest ice mass variations, climate cycles and climate change. *PNAS*, 109:11944—11948.

Bevis M., et al. (2019) Accelerating changes in ice mass within Greenland, and the ice sheet's sensitivity to atmospheric forcing. *PNAS*, 116(6):1934—1939.

Blank B., et al. (2021) Effect of lateral and temporal viscosity variations on GIA induced uplift rates in the Amundsen Sea Embayment. *Earth and Space Science Open Archive (ESSOAr)*, doi: 10.1002/essoar.10506643.1.

Briner J., et al. (2011) Varve and radiocarbon dating support the rapid advance of Jakobshavn Isbrae dring the Little Ice Age. *Quaternary Science Reviews* 30(19-20):2476—2486.

Briner J., et al. (2020) Rate of mass loss from the Greenland Ice Sheet will exceed Holocene values this century. *Nature* 586:70—74.

Cammarano F., et al. (2005) One-dimensional physical reference models for the upper mantle and transition zone: Combining seismic and mineral physics constraints. *Journal of Geophysical Research*, 110:B01306.

Caron L., et al. (2017) Inverting glacial isostatic adjustment signal using Bayesian framework and two linearly relaxing rheologies. *Geophysical Journal International*, 209: 1126—1147.

Caron L., et al. (2018) GIA model statistics for GRACE hydrology, cryosphere, and ocean science. *Geophysical Research Letter*, 45:2203—2212.

Conrad C. and Lithgow-Bertelloni C. (2006) Influence of continental roots and asthenosphere on plate-mantle coupling. *Geophysical Research Letters*, 33:L05312.

Cuzzone J., et al. (2019) The impact of model resolution on the simulated Holocene retreat of the southwestern Greenland ice sheet using the Ice Sheet System Model (ISSM). *The Cryosphere*, 13:879—893.

Darbyshire, F. et al. (2018) Crust and uppermost-mantle structure of Greenland and the Northwest Atlantic from Rayleigh wave group velocity tomography, *Geophysical Journal International*, 212:1546—1569.

Dziewonski A. and Anderson D. (1981) Preliminary reference Earth model. *Physics of the Earth and Planetary Interiors*, 25:297—356.

Farrell, W. (1972) Deformation of the Earth by surface loads. *Review of Geophysics*, 10(3):761—797.

Faul U. and Jackson I. (2015) Transient creep and strain energy dissipation: An experimental perspective. *Annual Review of Earth and Planetary Science*, 43: 541—569.

Fischer H., et al. (1998) Little ice age clearly recorded in northern Greenland ice cores. *Geophysical Research Letters*, 25(10):1749—1752.

Fleming K. and Lambeck K. (2004) Constraints on the Greenland Ice Sheet since the Last Glacial Maximum from sea-level observations and glacial-rebound models. *Quaternary Science Reviews*, 23:1053—1077.

French S. and Romanowicz B. (2014) Whole-mantle radially anisotropic shear-velocity structure from spectral-element waveform tomography. *Geophysical Journal International*, 199:1303—1327.

Grove, J. (1988) *The Little Ice Age*. London: Routledge, xxii + 498 pp.

Ivins E. and James T. (1999) Simple models for late Holocene and present-day Patagonian glacier fluctuations and predictions of a geodetically detectable isostatic response. *Geophysical Journal International*, 138:601—624.

Ivins E., et al. (2020) A linear viscoelasticity for decadal to centennial time scale mantle deformation. *Reports on Progress in Physics*, 83:106801.

Kelly M. and Lowell T. (2009) Fluctuations of local glaciers in Greenland during latest Pleistocene and Holocene time. *Quaternary Science Reviews*, 28(21—22):2088—2106.

Khan S., et al. (2014) Glacier dynamics at Helheim and Kangerdlugssuaq glaciers, southeast Greenland, since the Little Ice Age. *The Cryosphere*, 8:1497—1507.

Khan S., et al. (2015) Greenland ice sheet mass balance: a review. *Reports on Progress in Physics*, 78(4):046801.

Khan S., et al. (2016) Geodetic measurements reveal similarities between post-last glacial maximum and present-day mass loss from the Greenland Ice Sheet. *Science Advances*, 2(9):e1600931.

Khan S., et al. (2020) Centennial response of Greenland's three largest outlet glaciers. *Nature Communications*, 11:5718. Doi: 10.1038/s41467-020-19580-5.

Kjeldsen K., et al. (2015) Spatial and temporal distribution of mass loss from the Greenland Ice Sheet since AD 1900. *Nature*, 528:396—400.

Kohlstedt D. and Hansen L. (2015) Constitutive equations, rheological behavior, and viscosity of rocks. In *Treaties of Geophysics* (Schubert G., editor-in-chief), 2nd edition, vol. 2, Oxford: Elsevier, p. 441—472.

Lambeck K., et al. (2014) Sea level and global ice volumes from the Last Glacial Maximum to the Holocene. *PNAS*, 111(43):15296—15303.

Lambeck K., et al. (2017) The North American Late Wisconsin ice sheet and mantle viscosity from glacial rebound analyses. *Quaternary Science Reviews*, 158:172—210.

Larsen N., et al. (2015) The response of the southern Greenland ice sheet to the Holocene thermal maximum. *Geology*, 43(4):291—294.

Laske G., et al. (2013) Update on CRUST1.0 – A 1-degree global model of Earth's crust. *EGU General Assembly*, abstract id EGU2013-2658.

Lau H., et al. (2016) Inferences of mantle viscosity based on ice age data sets: Radial structure. *Journal of Geophysical Research Solid Earth*, 121:6991—7012.

Lau H. and Holtzman B. (2019) "Measures of dissipation in viscoelastic media" extended: Toward continuous characterization across very broad geophysical time scales. *Geophysical Research Letters*, 46:9544—9553.

Lau H., et al. (2020) Toward a self-consistent characterization of lithospheric plates using full-spectrum viscoelasticity. *AGU Advances*, 1:e2020AV000205.

Lea J., et al. (2014) Terminus-driven retreat of a major southwest Greenland tidewater glacier during the early 19th century: insights from glacier reconstructions and numerical modeling. *Journal of Glaciology*, 60(220):333—344.

Lecavalier B., et al. (2014) A model of Greenland ice sheet deglaciation constrained by observations of relative sea level and ice extent. *Quaternary Science Reviews*, 102:54—84.

Liu S., et al. (2020) Thin crème brûlée rheological structure for the Eastern California Shear Zone. *Geology*, 46, doi:10.1130/G47729.1.

Longman, I. (1962) A Green's function for determining the deformation of the Earth under surface mass loads: 1. Theory. *Journal of Geophysical Research*, 67:845—850.

Marzeion B., et al. (2015) Brief Communication: Global reconstructions of glacier mass change during the 20th century are consistent. *The Cryosphere*, 9:2399—2404.

Milne G., et al. (2018) The influence of lateral Earth structure on glacial isostatic adjustment in Greenland. *Geophysical Journal International*, 214(2):1252–1266.

Motyka R., et al. (2017) Asynchronous behavior of outlet glaciers feeding Godthåbsfjord (Nuup Kangerlua) and the triggering of Narsap Sermia's retreat in SW Greenland. *Journal of Glaciology*, 63(238): 288—308.

Mouginot J., et al. (2019) Forty-six years of Greenland Ice Sheet mass balance from 1972 to 2018. *PNAS*, 116(19): 9239—9244.

Muto J., et al. (2019) Coupled afterslip and transient mantle flow after the 2011 Tohoku earthquake. *Science Advances*, 5(9):eaaw1164.

Nield G., et al. (2014) Rapid bedrock uplift in the Antarctic Peninsula explained by viscoelastic response to recent ice unloading. *Earth and Planetary Science Letters*, 397:32—41.

Nilsson J., et al. (2016) Improved retrieval of land ice topography from CryoSat-2 data and its impact for volume-change estimation of the Greenland Ice Sheet. *The Cryosphere*, 10: 2953—2969.

Noël B., et al. (2016) A daily, 1 km resolution data set of downscaled Greenland ice sheet surface mass balance (1958—2015). *The Cryosphere*, 10:2361—2377.

Peltier W., et al. (2015) Space geodesy constrains ice age terminal deglaciation: The global ICE6G_C (VM5a) model. *Journal of Geophysical Research Solid Earth*, 120:450—487.

Pfeffer W., et al. (2014) The Randolph Glacier Inventory: a globally complete inventory of glaciers. *Journal of Glaciology*, 60(221): 537—552.

Pollitz F. (2019) Lithosphere and shallow asthenosphere rheology from observations of post-earthquake relaxation. *Physics of the Earth and Planetary Interiors*, 293:106271.

Pourpoint M., et al. (2018) Lithosphere structure of Greenland from ambient noise and earthquake surface wave tomography. *Journal of Geophysical Research Solid Earth*, 123:7850—7876.

Ritsema J., et al. (2011) S40RTS: a degree-40 shear-velocity model for the mantle from new Rayleigh wave dispersion, teleseismic travel time and normal-mode splitting function measurements. *Geophysical Journal International*, 184(3):1223—1236.

Sasgen I., et al. (2020) Return to rapid ice loss in Greenland and record loss in 2019 detected by the GRACE-FO satellites. *Communications Earth & Environment*, 1(8): https://doi.org/10.1038/s43247-020-0010-1.

Schaeffer A. and Lebedev S. (2013) Global shear speed structure of the upper mantle and transition zone. *Geophysical Journal International*, 194:417—449.

Simpson M., et al. (2009) Calibrating a glaciological model of the Greenland ice sheet from the Last Glacial Maximum to present-day using field observations of relative sea level and ice extent. *Quaternary Science Reviews*, 28:1631—1657.

Simpson M., et al. (2011) The influence of decadal- to millennial-scale ice mass changes on present-day vertical land motion in Greenland: Implications for the interpretation of GPS observations. *Journal of Geophysical Research*, 116:B02406.

Steffen R., et al. (2018) Weakened lithosphere beneath Greenland inferred from effective elastic thickness: a hotspot effect? *Geophysical Research Letters*, 45(10):4733—4742.

Tarasov L. and Peltier, W. (2002) Greenland glacial history and local geodynamic consequences. *Geophysical Journal International*, 150:198—229.

Tarasov L., et al. (2012) A data-calibrated distribution of deglacial chronologies for the North American ice complex from glaciological modeling. *Earth and Planetary Science Letters*, 315—316:30—40.

The IMBIE Team. (2020) Mass balance of the Greenland Ice Sheet from 1992 to 2018. *Nature*, 579:233—239.

van Dam T., et al. (2017) Using GPS and absolute gravity observations to separate the effects of present-day and Pleistocene ice-mass changes in South East Greenland. *Earth and Planetary Science Letters*, 459:127—135.

Velicogna I., et al. (2020) Continuity of ice sheet mass loss in Greenland and Antarctica from the GRACE and GRACE Follow-On missions. *Geophysical Research Letters*, 47:e2020GL087291.

Wake L., et al. (2016) Glacial Isostatic Adjustment (GIA) in Greenland: a review. *Current Climate Change Reports*, 2:101—111.

Watkins M., et al. (2015) Improved methods for observing Earth's time variable mass distribution with GRACE using spherical cap mascons. *Journal of Geophysical Research*, 120:2648—2671.

Woodroffe S., et al. (2017) Saltmarsh record of post Little Ice Age mass balance changes in Southeast Greenland. *AGU Fall Meeting*, abstract id C11B-0912.

Wouters B., et al. (2019) Global glacier mass loss during the GRACE satellite mission (2002-2016). *Frontiers in Earth Science*, 7:96.

Zhang B., et al. (2019) Geodetic and model data reveal different spatio-temporal patterns of transient mass changes over Greenland from 2007 to 2017. *Earth and Planetary Science Letters*, 515:154—163.

Zhong S., et al. (2003) Three-dimensional finite element modeling of Earth's viscoelastic deformation: effects of lateral variations in lithospheric thickness. *Geophysical Journal International*, 155:679—695.

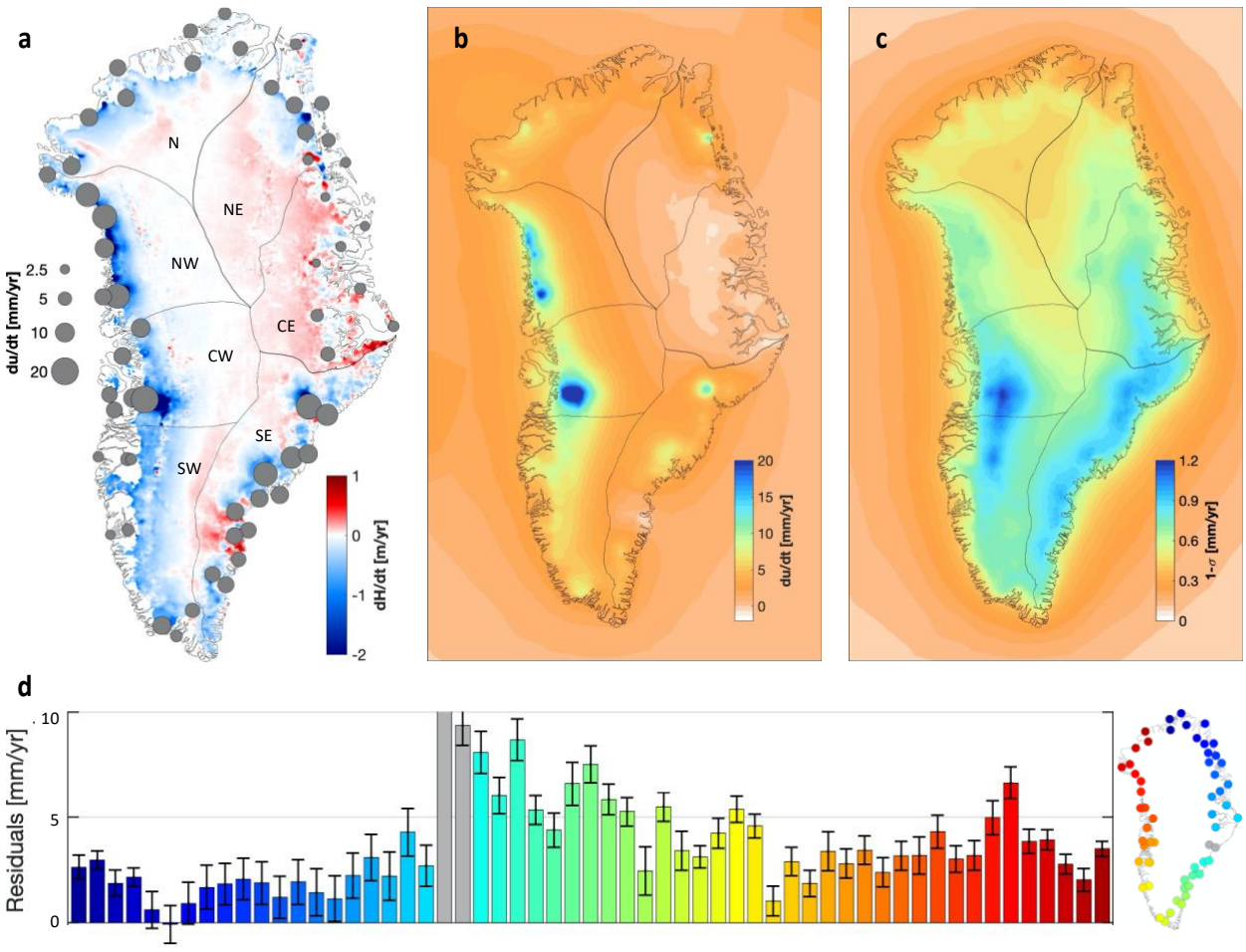

Figure 1. Observed and modeled uplift rates and the residuals. (a) The positions of 57 GNSS stations are shown with gray circles, whose size represents the average rate of crustal uplift, du/dt, measured during 2011–2016. The uplift rate is computed by removing the seasonal signal from the GNSS timeseries and fitting the residual with a quadratic polynomial. The background map shows the mean rate of ice thickness change, dH/dt, during the same period. Following Kjeldsen et al. (2015), we outline seven regions for which the so-called GIA corrections are estimated for GRACE and GRACE-FO missions (Supplementary Table S1). Labels refer to north (N), northeast (NE), northwest (NW), central east (CE), central west (CW), southeast (SE) and southwest (SW). **(b)** Mean and **(c)** 1-σ uncertainty of elastic uplift rates induced by present-day ice thickness change. **(d)** Residual uplift rates at the GNSS stations, derived by subtracting the sum of the elastic and GIA uplift rates from the measured rates. Two stations located near Kangerlussuaq Glacier (gray circles in the right-side inset), whose residuals are shown with gray bars, are excluded from further analysis because their measurements are thought to be affected by the passage of the Icelandic hotspot (Khan et al., 2016), a feature not treated here.

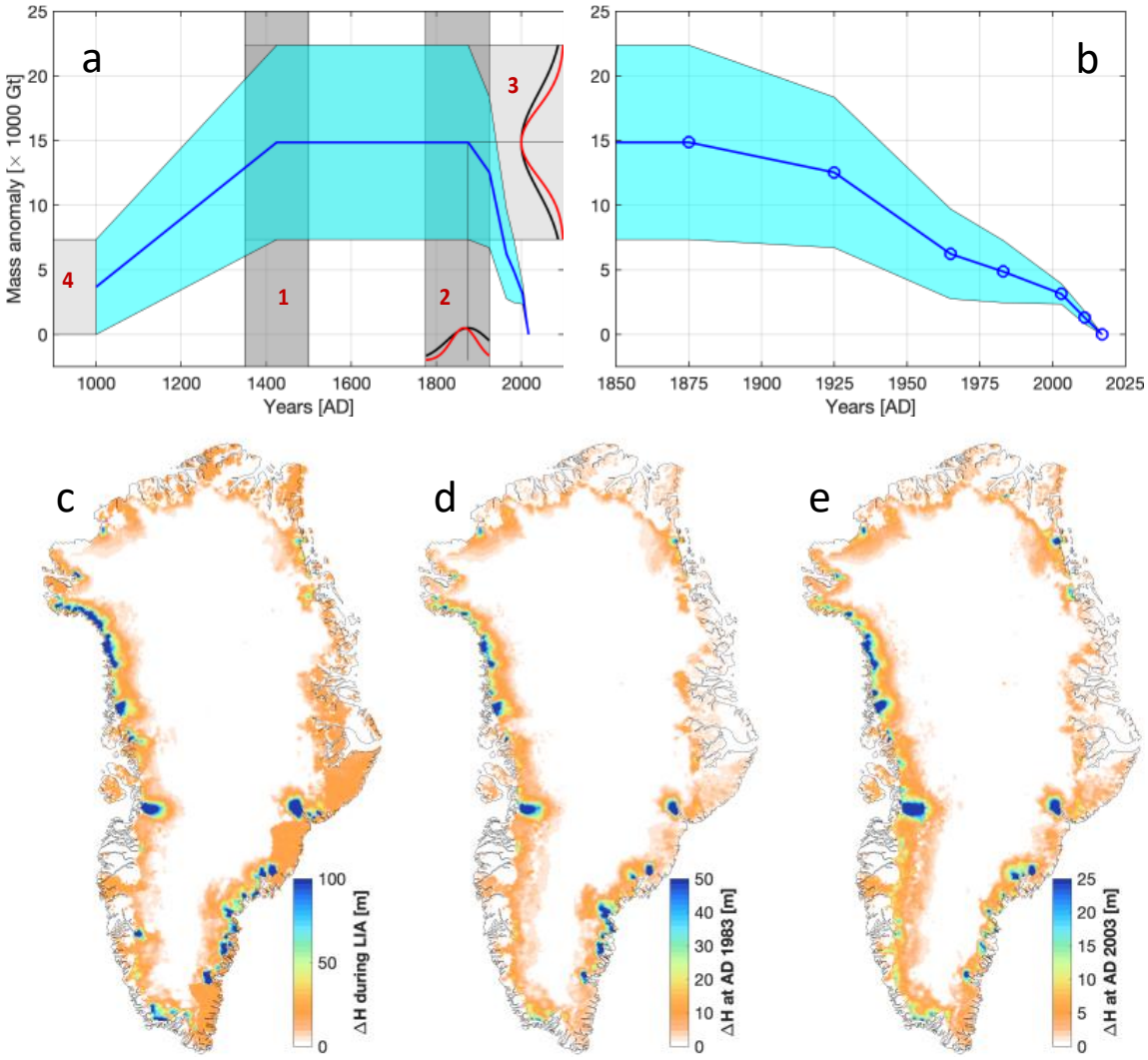

Figure 2. Post-MWP loading history considered in our Bayesian exploration. (a) Summary of ice load history and uncertainty therein. Free parameters 1 and 2 (shown with vertical shadows) determine the inception and termination timing of the LIA, respectively, and parameters 3 and 4 (horizontal shadows) are related to the amplitude of the mass anomaly during the LIA and MWP, respectively. A priori likelihood is imposed for parameters 2 and 3; black and red Gaussian functions show, respectively, the prior and (normalized) posterior probabilities. **(b)** A zoom-in of the loading history over the past 170 years. **(c-e)** Spatial distribution of ice thickness anomaly, relative to AD 2016, at select times: during the LIA maximum, at AD 1983 and 2003, respectively.

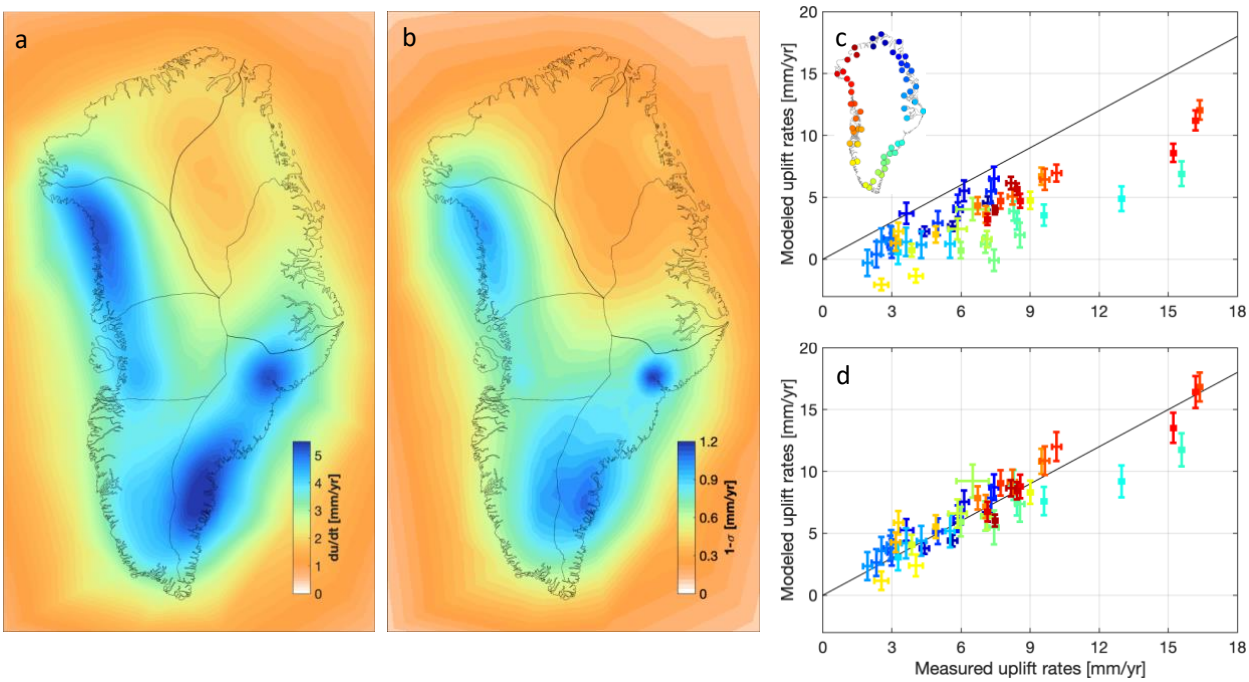

Figure 3. Crustal uplift rates due to the post-MWP loading and improvements to GNSS data fit. (a) Expected uplift rates due to the post-MWP loading history and **(b)** associated uncertainties inferred from our Bayesian analysis. **(c)** The summed elastic and GIA uplift rates plotted against the measured GNSS uplift rates at 55 GNET stations. **(d)** Same as **c** but after adding the post-MWP load induced uplift rates to the modeled rates. Notice the improvement to data fit and an overall reduction in data variance.

Supplementary Materials for

Reconciliation of the paleo sea-level record with modern crustal uplift of Greenland

by Surendra Adhikari and Colleagues.
Jet Propulsion Laboratory, California Institute of Technology.

This document includes the following items.

Figures.

Table.

Additional references.

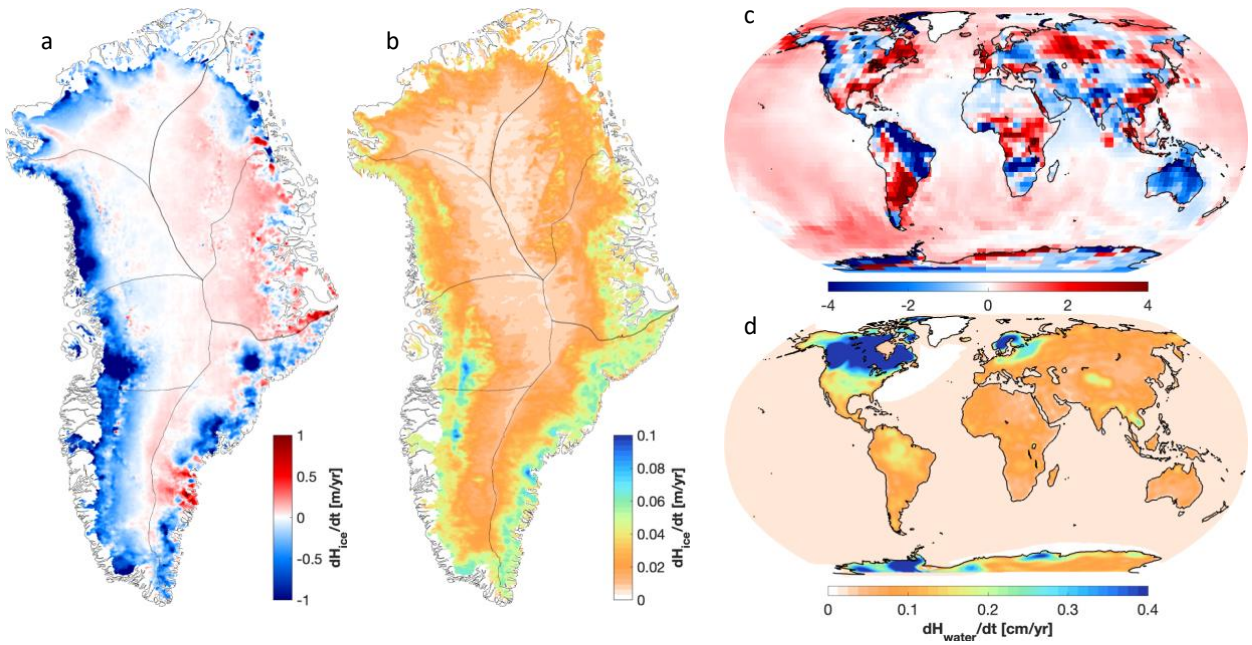

Figure S1. Contemporary surface loads considered for modeling elastic uplift rates. (a) Mean and (b) standard deviation of measured ice thickness change during 2011-2016. (c) Mean and (d) standard deviation of intermediate and farfield mass change during the same time period.

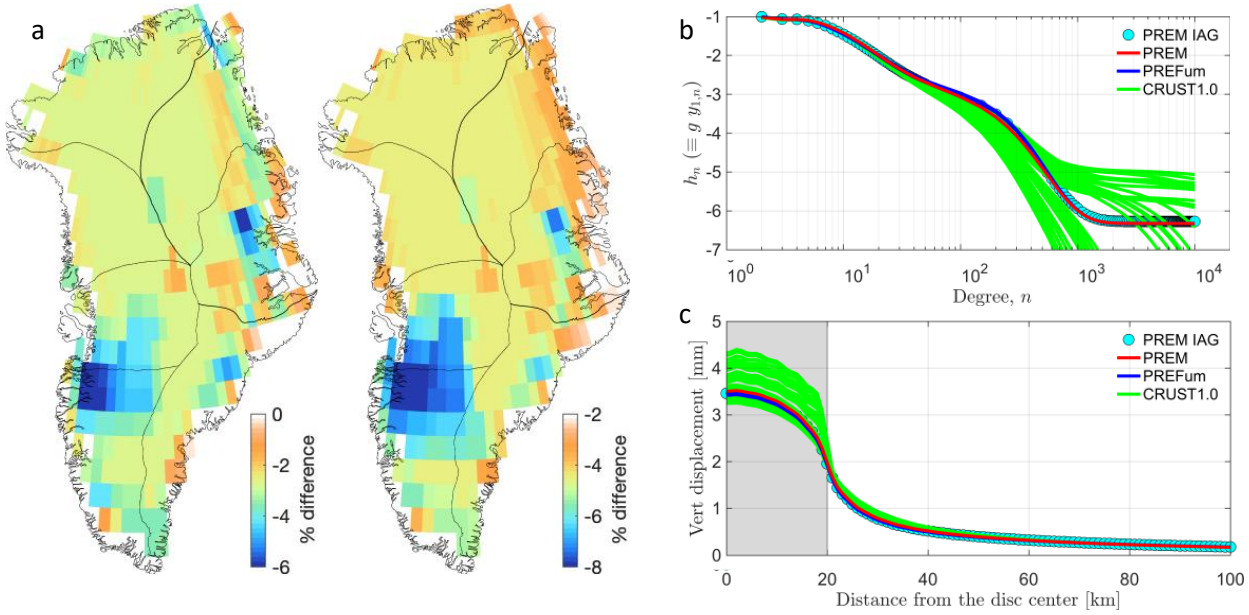

Figure S2. Regional elastic Earth structure in Greenland and its effect on the modeled uplift. (a) Percent deviation of CRUST1.0 solutions, relative to PREM, for density (left) and Poisson's ratio (right), averaged over upper 50 km depth. **(b)** Our estimates of loading love numbers h_n up to degree $n = 10{,}000$ computed for PREM (Dziewonski and Anderson, 1981), PREFum (Cammarano et al., 2005) and CRUST1.0 profiles (Laske et al., 2013). Our solutions compare well against the solutions provided by the International Association of Geodesy (IAG) for PREM (see red line versus cyan circles). **(c)** Modeled bedrock displacement profiles in response to the unloading of 1-m thick water table from a disc of 20 km radius. The models featuring CRUST1.0 profiles generally yield larger displacement than PREM.

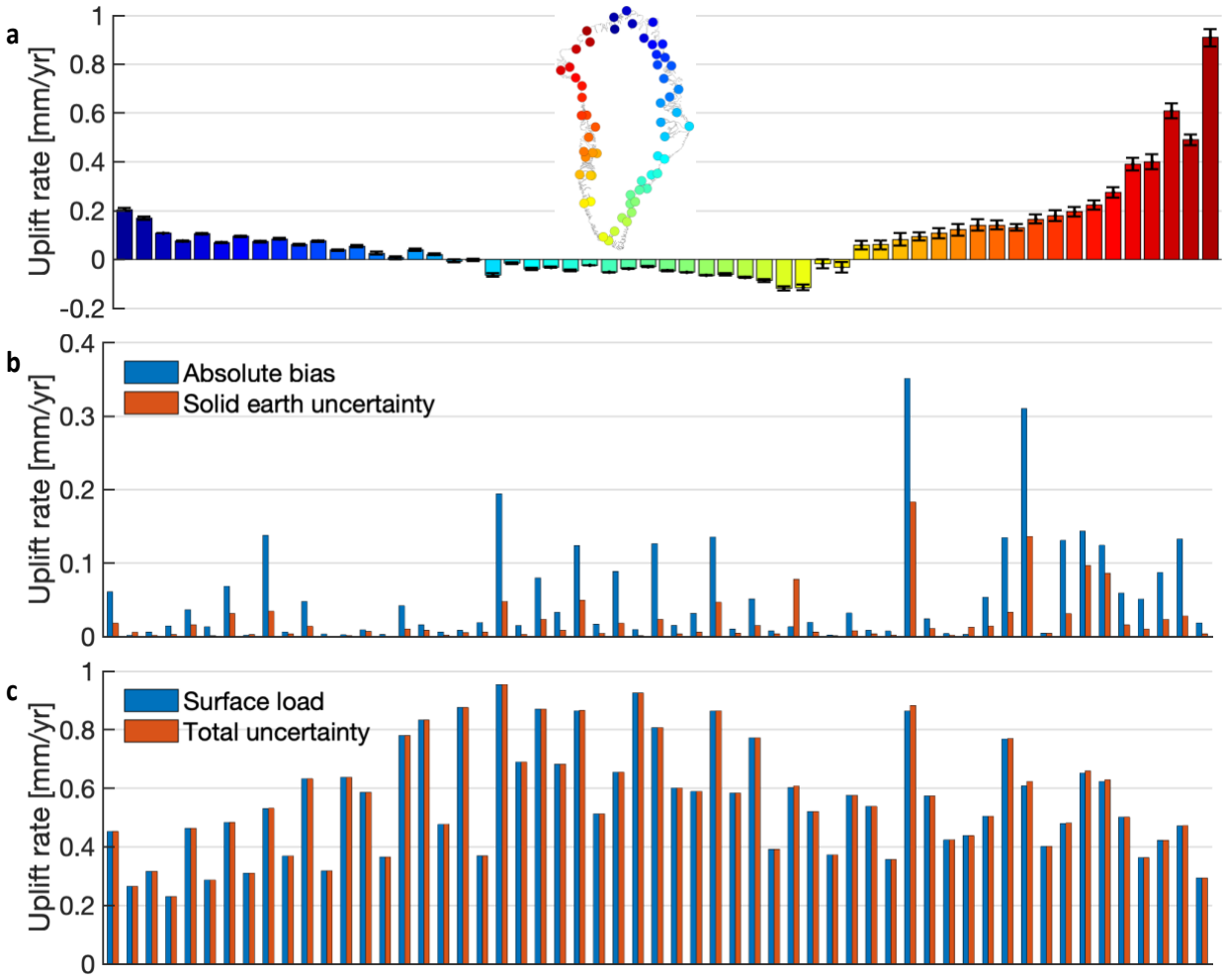

Figure S3. A diagnostic of the modeled elastic uplift rates. (a) Modeled uplift rates at GNET stations due to the intermediate and farfield surface mass changes. **(b)** The bias and uncertainty associated with the elastic Earth structure at GNET stations. The bias is defined as the difference between our estimate of mean elastic uplift rates (Figure 2b in the main text) and that derived from PREM. We generally find a positive bias at many GNET stations (see Figure S2c). The uncertainty is derived from an ensemble of 640 CRUST1.0 profiles. **(c)** Surface load related uncertainty dominates the total uncertainty in the modeled uplift rates. The order of GNSS stations in the latter two panes is same as shown in panel **a**.

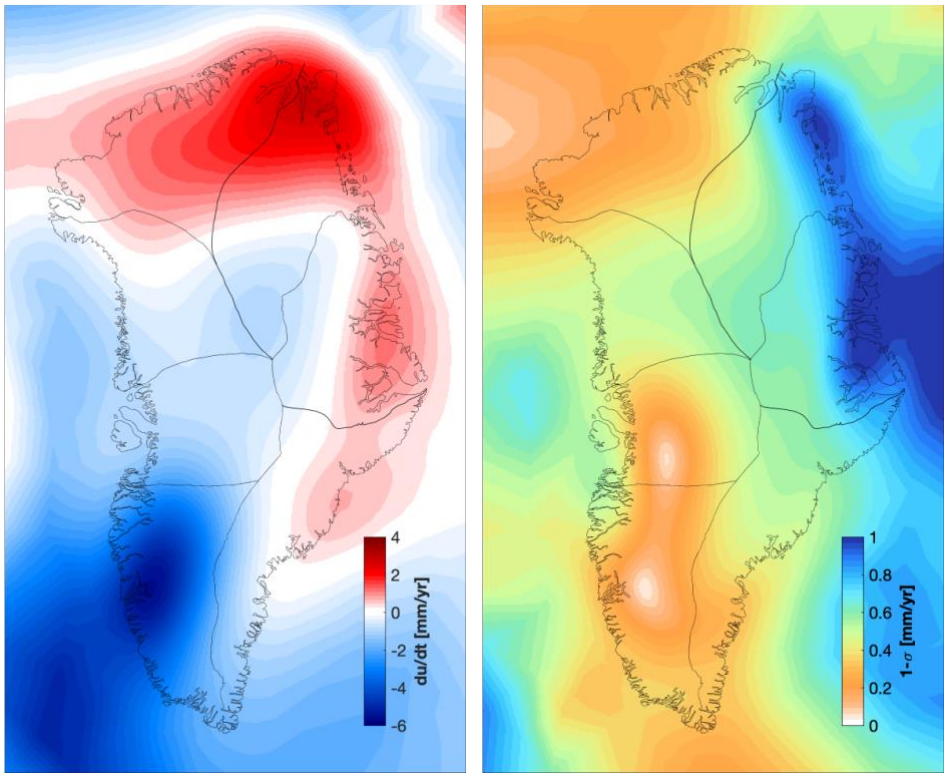

Figure S4. Modeled GIA uplift rates and uncertainties therein. These solutions are based on eight 3-D Earth models that include lateral heterogeneity in lithosphere thickness and mantle viscosity (taken from Milne et al., 2018). The uncertainty estimate, however, does not account for that associated with the deglacial history. The largest uncertainties (*Ø*1 mm/yr) are found in the northeast, where the models of 3-D mantle viscosity exhibit considerable disagreement.

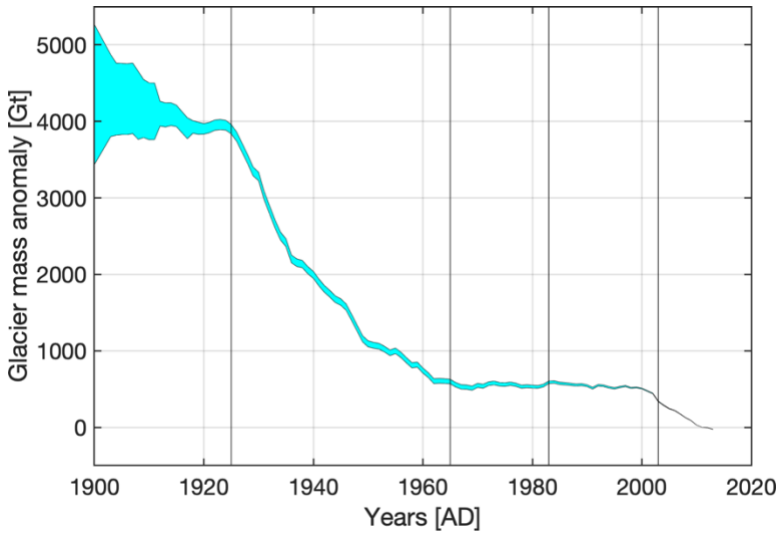

Figure S5. Cumulative mass loss from Greenland peripheral glaciers since AD 1900. The cyan envelope shows the reconstructed mass anomaly, relative to AD 2011, within 1-sigma uncertainty (taken from Marzeion et al. 2015). For our modeling purpose, we assume linear change in mass over the period: LIA-1925, 1925-1965, 1965-1983, 1983-2003, 2003-2011 (see Figure 2 in the main text).

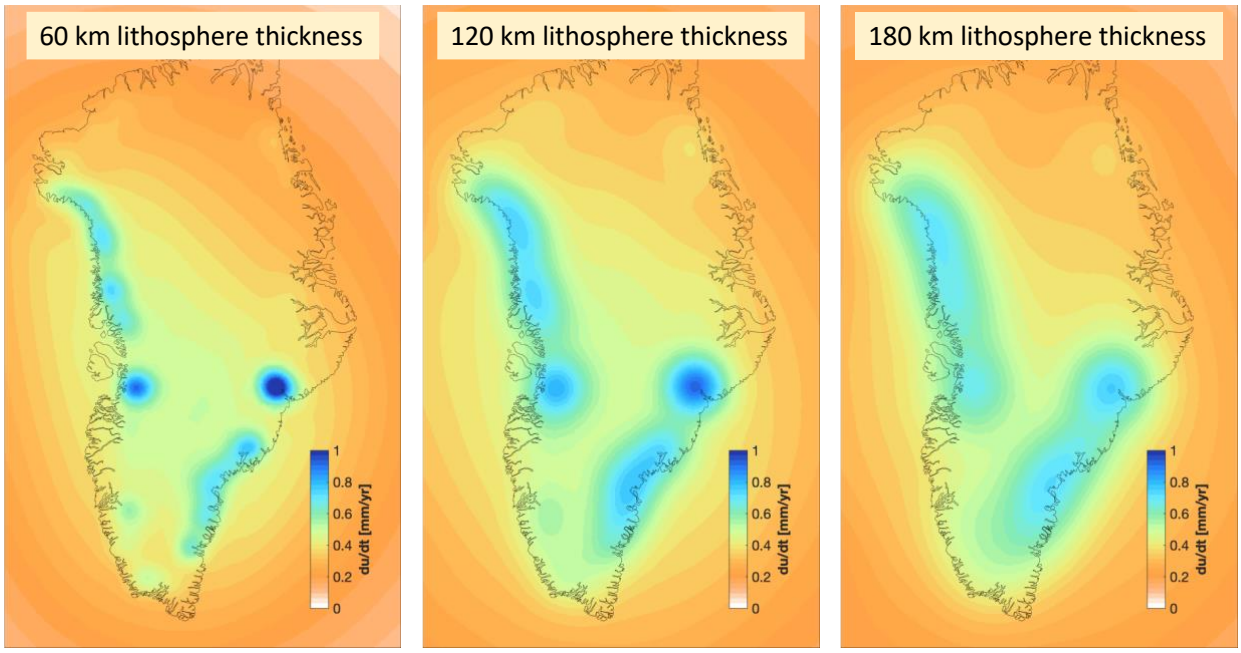

Figure S6. Crustal uplift rates due to post-MWP load changes computed using a GIA model. We use a half-space Maxwell Earth model (Ivins and James, 1999; Adhikari et al., 2014) with a typical Greenland upper mantle viscosity, 5×10^{20} Pa s (Simpson et al., 2009; Lecavalier et al., 2014), and consider three plausible lithosphere thicknesses.

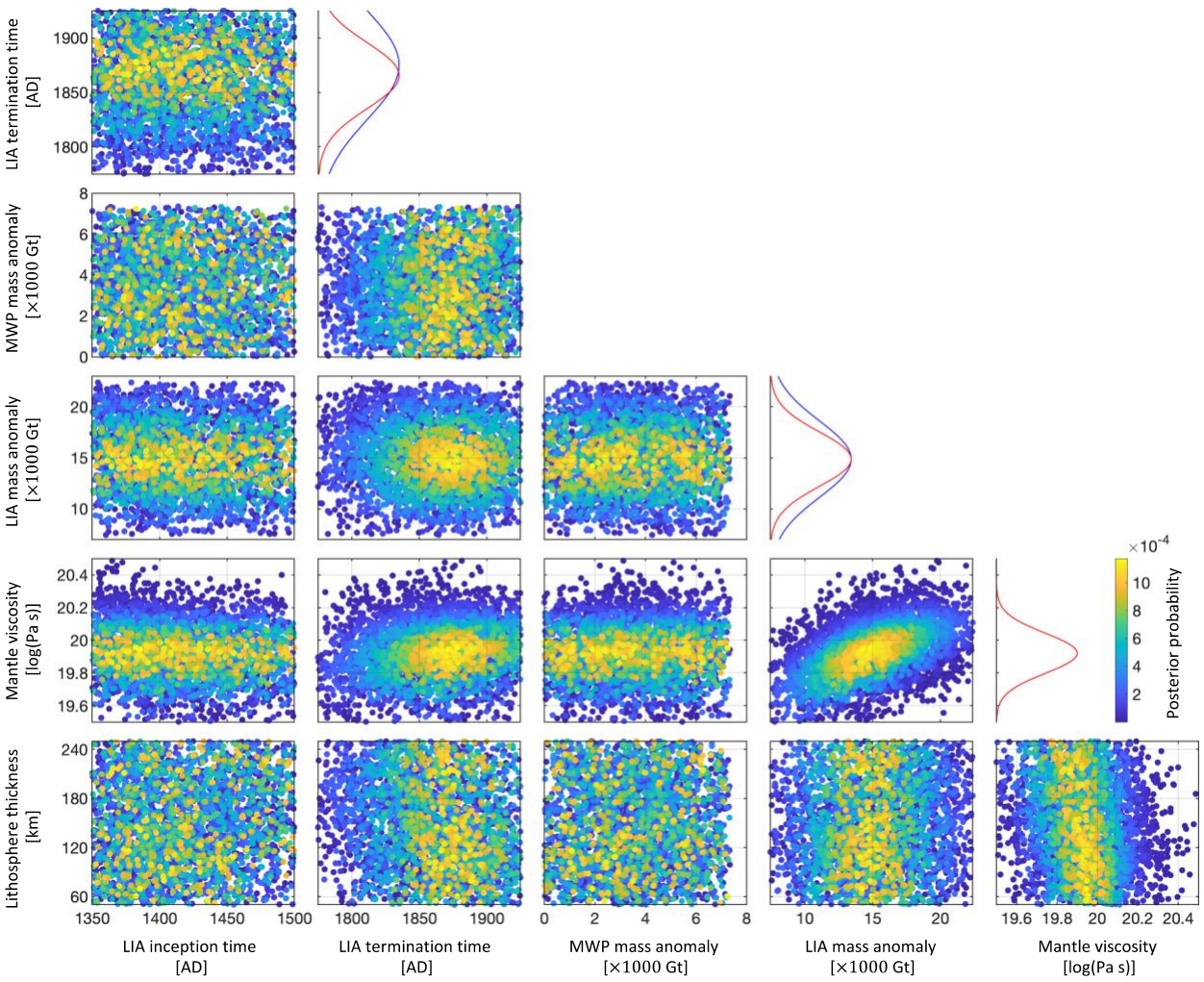

Figure S7. Posterior probability distribution in 2-D spaces formed by each pair of parameters. Gaussian priors are imposed for the LIA termination time and the LIA mass anomaly (blue lines), while for other parameters uniform priors are considered. Posterior probability distributions are shown for select parameters (red lines). Note that model parameter values with higher posterior probability are plotted on top of other values for clarity.

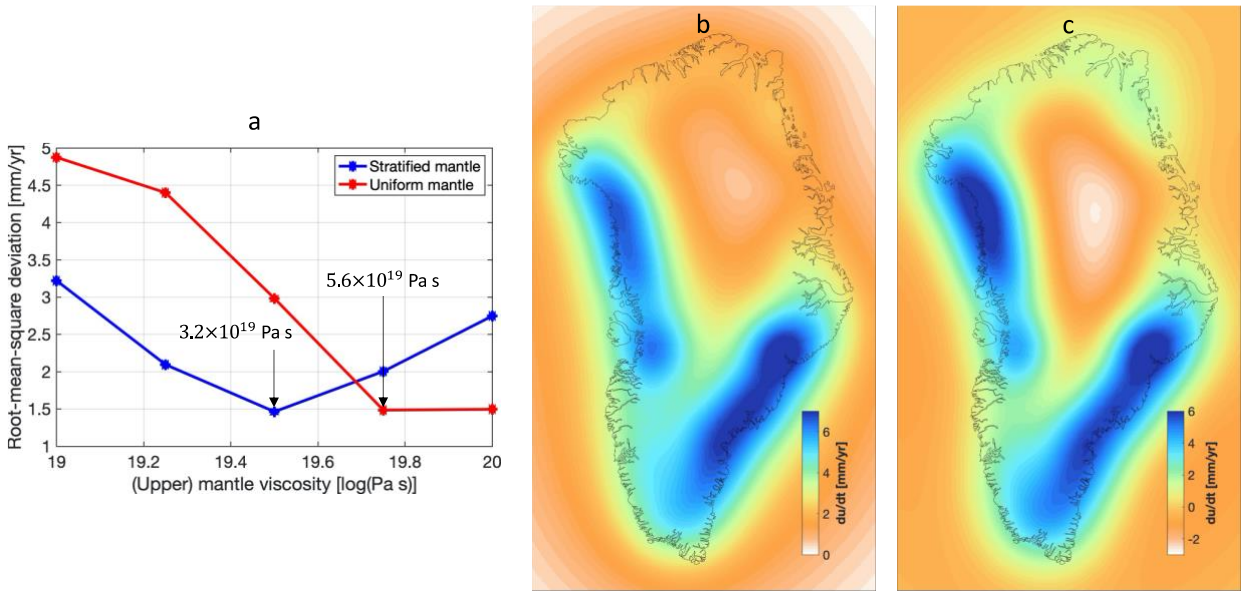

Figure S8. Crustal uplift rates due to post-MWP load changes based on a 3-layer spherical Earth model. We use a 3-layer spherical Earth model featuring 120-km thick lithosphere and two mantle layers (Caron et al., 2018) and force it by the deglacial history since AD 1000 (see Figure 2 in the main text). The deglaciation parameters are constrained by the Bayesian analysis performed using a half-space Earth model (see Supplementary Figure S7). First, we run five simulations with the same upper and lower mantle viscosities that vary in the range between 19 and 20 log(Pa s). The goal here is to test whether the isoviscous simulation of a spherical Earth model reproduces the half-space model solution. Next, we run additional five simulations wherein we let the upper mantle viscosity vary and keep the lower mantle viscosity fixed at a value typically used in Greenland GIA studies (2×10^{21} Pa s, Lecavalier et al., 2014). The goal here is to test the impact of mantle stratification on the inferred (upper) mantle viscosity. **(a)** Root-mean-square deviation (RMSD) as a function of (upper) mantle viscosity. RMSD is computed based on the modeled and residual uplift rates (Figure 1d in the main text). For the isoviscous mantle, the smallest RMSD is found with the viscosity value of $6 - 10 \times 10^{19}$ Pa s, comparable to the inference based on the half-space Earth model. For the stratified mantle, the smallest RMSD is found with the upper mantle viscosity value of 3×10^{19} Pa s. The model with a stratified mantle prefers smaller upper mantle viscosity than the isovicous model, at least by a factor of 2. **(b-c)** Modern uplift rates predicted by the isoviscous and stratified mantle models, respectively.

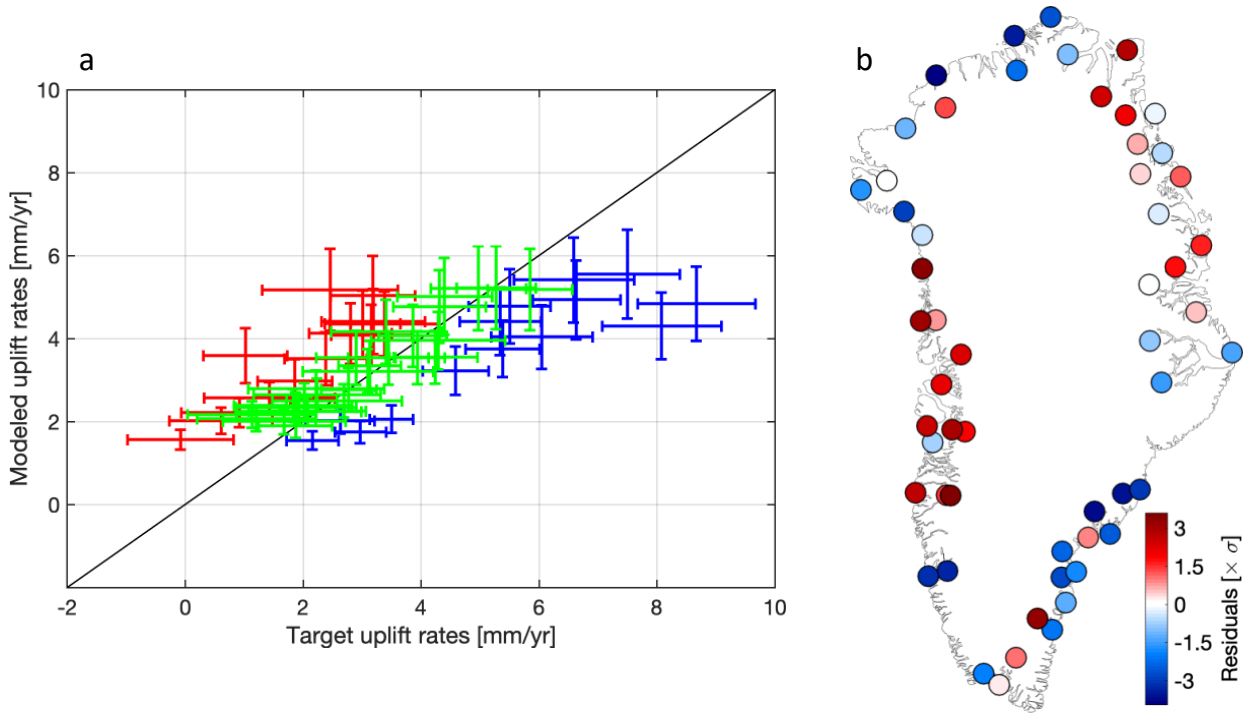

Figure S9. Data-model misfit at GNET stations. (a) Modeled uplift rates due to the post-MWP load changes compared against the target values (see Figure 1d in the main text). While the model predicts uplift rates within 1-σ uncertainty of target values at several GNET stations (green crosses), it overpredicts (underpredicts) at several other stations as denoted by red (blue) crosses. **(b)** Spatial pattern of data-model misfit normalized by 1-σ values of target uplift rates at GNET stations. Stations with larger misfit are distributed all along the coast. However, a systematic spatial structure is apparent: the model generally overpredicts in the central west and northeast and underpredicts in the south and the north.

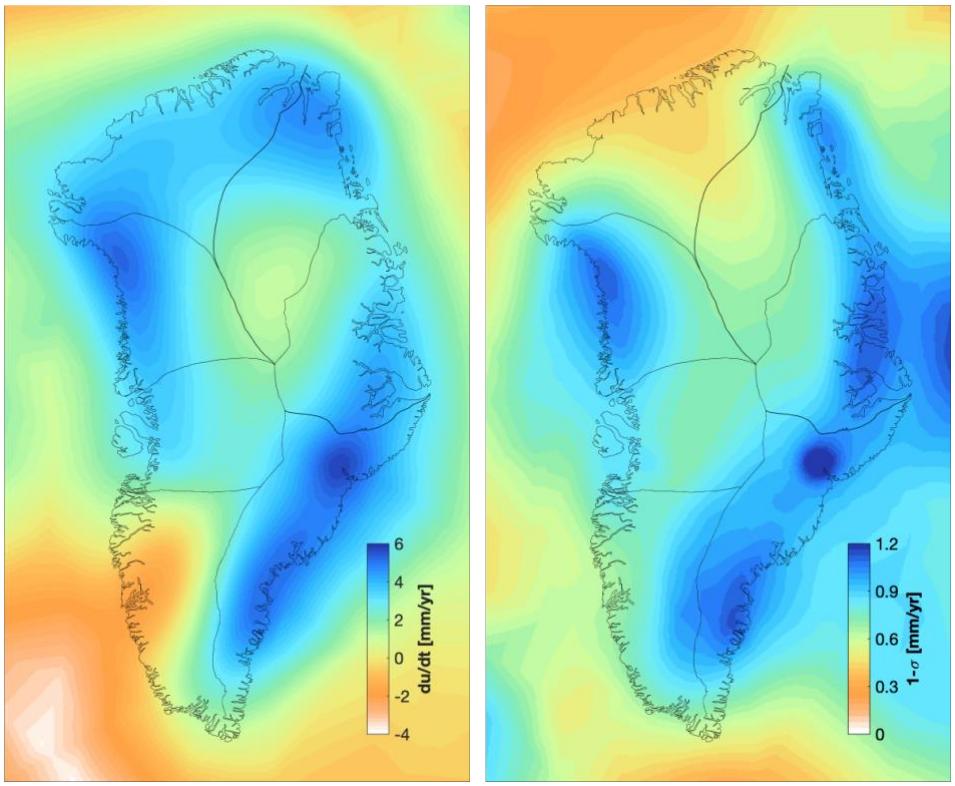

Figure S10. Viscous component of modeled uplift rates and uncertainty. These results are derived by combining uplift rates associated with the Holocene deglaciation (Supplementary Figure S4) and those associated with the post-MWP load changes (figures 3a-b in the main text).

Supplementary Table S1. Regional ice sheet mass balance correction for GRACE and GRACE-FO missions. Since modeled geoid perturbations induced by post-MWP load changes evolve rather mildly (by about 10% at most) during the GRACE/GRACE-FO observing period, we may assume a constant rate and quantify its time-averaged contribution to ice sheet mass balance following the same method as applied for the so-called GRACE GIA correction (e.g., Ivins et al., 2011). The regional boundaries are outlined in Figure 1a in the main text. Units are Gt/year.

	SW	CW	NW	N	NE	CE	SE	Greenland
Post-MWP	4.4 ± 0.9	3.4 ± 0.7	3.7 ± 0.7	3.1 ± 0.6	2.4 ± 0.4	3.1 ± 0.5	5.0 ± 1.0	25.1 ± 4.7
GIA	-3.8 ± 0.3	-0.8 ± 0.4	-0.3 ± 0.5	1.7 ± 0.4	0.8 ± 0.7	0.3 ± 0.8	-0.3 ± 0.5	-2.4 ± 3.7
Total	0.6 ± 0.9	2.6 ± 0.8	3.4 ± 0.9	4.8 ± 0.7	3.2 ± 0.8	3.4 ± 0.9	4.7 ± 1.1	22.7 ± 6.1

Additional references.

Ivins E., et al. (2011) On-land ice loss and glacial isostatic adjustment at the Drake Passage: 2003-2009. *Journal of Geophysical Research Solid Earth*, 116:B02403.